Supporting Information

Zhuang Cheng [a], *Xin He* [b], *Hui Liu* [a], *Shuyuan Ge* [a], *Yixuan Jiang* [a], *Futong Liu* [a], *Ping Lu* [a,]*

[a] State Key Laboratory of Supramolecular Structure and Materials, College of Chemistry, Jilin University, Changchun, 130012 P. R. China

[b] College of Physics, Jilin University, Changchun, 130012 P. R. China

E-mail: lup@jlu.edu.cn.

Table of Contents

1. Experimental Section

1.1 General information

All the reagents and solvents are used as received without further purification. ^{1}H NMR was recorded by Bruker AVANCE 500 spectrometer at 500 MHz, 126 MHz and 160 MHz with tetramethylsilane (TMS) as the internal standard. On a Flash EA 1112, CHNS-O elemental analysis instrument, elemental analysis was performed. An AXIMACFRTM plus apparatus produced MALDI-TOF-MS mass spectra. On a Perkin-Elmer thermal analysis equipment, thermal gravimetric analysis (TGA) was carried out between 30 and 900 °C. The NETZSCH (DSC-204) machine recorded differential scanning calorimetry (DSC) from 30 to 400 °C. Thermal evaporation in high vacuum was used to create organic films for optical measurements on clear quartz surfaces. Spectra in the UV-Vis range were captured using a Shimadzu UV-3100 spectrophotometer. With the use of an RF-5301PC spectrophotometer, steady state photoluminescence spectra were measured. The Edinburgh spectrometer LP920 was used to collect time-resolved photoluminescence spectra using a 365-nm laser flash as the excitation source. Using a FLS920 spectrometer and a 375-nm picosecond pulsed light-emitting diode excitation source (pulse width: 898.1 ps), the PL lifetime was determined. The integrating sphere was used to calculate the PLQY. To determine emitting dipole orientation of an emitting film, angle-resolved and polarization-resolved PL measurements were performed. The sample consisted of a fused silica substrate with the neat film of 30 nm. The sample was attached to a fused silica half-cylinder prism by index matching liquid. The excitation of the samples was performed with the 325-nm line of the continuous-wave He: Cd laser with a fixed excitation angle of 45°. The emission angle was changed by use of an automatic rotation stage. The spectra were resolved by utilization of a p-polarizing filter and measured by a fiber optical spectrometer. The angle-dependent p-polarized emission intensity at the peak wavelength of the PL spectrum of the emitting layer was detected.

1.2 Electrochemical measurements

Cyclic voltammetry (CV) was measured by using BAS 100B/W electrochemical analyzer with standard one-compartment, three-electrode electrochemical cell. The

working electrode was a glass-carbon disk electrode. The counter electrode was a Pt wire. The reference electrode was Ag/Ag^+. Ferrocenium/ferrocene (Fc^+ /Fc) redox couple was used as the internal standard and the formal potential of Fc^+ /Fc was 4.8 eV below vacuum. All potentials relative to Ag/Ag^+ electrode obtained from CV measurement were eventually referenced against Fc^+/Fc to calculate HOMO/LUMO levels. As a result, the Ag/Ag^+ electrode was just a pseudo reference. The HOMO/LUMO levels were calculated according to the following formalism:

$$E_{HOMO} = - (E_{ox} \text{ vs.} Fc^+/Fc + 4.8) \text{ eV} \qquad \text{Equation S1}$$

$$E_{LUMO} = - (E_{red} \text{ vs.} Fc^+/Fc + 4.8) \text{ eV} \qquad \text{Equation S2}$$

where the E_{ox} vs. Fc^+/Fc and E_{red} vs. Fc^+/Fc were oxidation and reduction onset potentials relative to Fc^+/Fc reference, respectively.

1.3 Device fabrications and measurements

ITO coated glasses with a sheet resistance of 20 Ω $square^{-1}$ were used as the substrate and cleaned by deionized water, isopropyl alcohol, acetone and toluene. Then the ITO glasses were irradiated in UV-zone for 30 min. The deposition system for organic and metal deposition has a base pressure lower than 5×10^{-6} mbar. The hole injecting layer HAT-CN was deposited at 0.1 Å s^{-1}. The deposition rate of all other organic layers was 1.0 Å s^{-1}. The electron injecting layer LiF was deposited at a rate of 0.1 Å s^{-1} and then the capping Al metal layer was deposited at a rate of 4.0 Å s^{-1}. The EL characteristics were measured under ambient condition at room temperature, using a Keithley 2400 programmable electrometer and CS-200 chromameter. EL spectra were collected on a PR-655 Spectro-scan spectrometer.

1.4 Theoretical calculations method

In order to obtain molecular geometries, the ground-state (S_0) and lowest singlet excited state (S_1) geometries were optimized at the B3LYP/6-31G (d, p) level. The optimized result was in good agreement with the experiment's findings. The optimized S_0 state was used to determine the HOMO/LUMO distributions. On the basis of the optimized configuration of S_0, the high excitation energy levels of the singlet and triplet states were computed using the TD-M062X/6-31G (d, p). Natural transition orbitals (NTOs) were assessed for the ten lowest excited levels, including singlet and triplet states under

TD-M062X/6-31G (d, p), with the goal of examining the attributes of excited states. By diagonalizing the transition density matrix linked to each excitation, this method offered the most condensed representation of the electronic transitions in terms of an expansion into single particle orbitals.

1.5 Calculation formulas for the photophysical parameters.

The calculation of the kinetic parameters assumes that internal conversion process of the singlet exciton is the main nonradiative decay.

$$k_p = 1/\tau_p \quad \text{Equation S3}$$

$$k_d = 1/\tau_d \quad \text{Equation S4}$$

$$k_r = \varphi_p k_p \quad \text{Equation S5}$$

$$k_{nr} = k_p - k_{ISC} - k_r \quad \text{Equation S6}$$

$$k_{ISC} = k_p \varphi_d/(\varphi_d+\varphi_p) \quad \text{Equation S7}$$

$$k_{RISC} = (k_p k_d)/(k_p - k_{ISC}) \quad \text{Equation S8}$$

Where τ_p is the lifetime of prompt fluorescent, τ_d is the lifetime of TADF, φ_p is the prompt fluorescent component of Φ_{PL}, φ_d is the delayed fluorescent component of Φ_{PL}. k_r is the radiative rate. k_{nr} is the nonradiative rate; k_{ISC}, k_{RISC} are the rate constants of intersystem crossing and reverse intersystem crossing, respectively.

1.6 Synthetic procedures

All the reagents and solvents used for the syntheses were purchased from Aldrich and Acros and used as received.

2. Supplementary Figures and Tables

2.1 Synthesis and characterization

Synthesis of 3-bromoacetonaphtho[1,2-b]pyrazine-8,9-dicarbonitrile (APBr):

5-Bromoacetylnaphthalene-1,2-dione (5.22 g, 20 mmol) and diaminomaleonitrile (2.38 g, 22 mmol) were placed in a 250 mL round-bottomed flask and 100 mL of glacial acetic acid was added as a solvent. The reaction was refluxed under nitrogen protection for 8 hours at a reaction temperature of 125 ℃. At the end of the reaction, it was poured into 100 mL of ice water and filtered to obtain the filter cake. The obtained crude product was washed with water and ethanol and dried to give a yellow powder (5.66 g, 85% yield). ^{1}H NMR (500 MHz, CD_2Cl_2, 25 °C, TMS) δ (ppm): 8.61 (d, J = 7.1 Hz, 1H; Ar H), 8.53 (d, J = 8.4 Hz, 1H; Ar H), 8.39 (d, J = 7.6 Hz, 1H; Ar H), 8.39 (d, J = 7.6 Hz, 1H). 7.6 Hz, 1H; Ar H), 8.23 (d, J = 7.5 Hz, 1H; Ar H), 8.09 (t, J = 7.7 Hz, 1H; Ar H). MALDI-TOF MS (mass m/z): calcd for $C_{16}H_5BrN_4$, 331.97; found, 331.35 [M^+].

Synthesis of 3-(4-(9,9-diphenylacridin-10(9H)-yl)phenyl)acetonaphtho[1,2-b]pyrazine-8,9-dicarbonitrile (DPAC-AP):

DPACB (2.68 g, 5 mmol), APBr (1.83 g, 5.5 mmol) and palladium tetrakis(triphenylphosphine) (173 mg, 0.15 mmol) were added to a 100 mL round-bottomed flask, followed by 40 mL of toluene and 20 mL of potassium carbonate solution at a concentration of 2.0 M. The reaction was carried out at reflux for 36 h under nitrogen protection at 90 °C. The reaction was extracted three times directly with dichloromethane solution at the end of the reaction, and the organic layers were combined and concentrated, followed by column chromatographic separation (eluent was petroleum ether: dichloromethane = 1:2). The crude product was recrystallized in ethanol and dried to give a yellow-orange solid (2.68 g, 81% yield). ^{1}H NMR (500 MHz, CD_2Cl_2, 25 °C, TMS) δ (ppm): 8.68 (d, J = 7.3 Hz, 1H; Ar H), 8.65 (d, J = 7.0 Hz, 1H; Ar H), 8.54 (d, J = 8.4 Hz, 1H; Ar H). Hz, 1H; Ar H), 8.09 (d, J = 7.3 Hz, 1H; Ar H), 8.06 (m, 1H; Ar H), 7.89 (d, J = 8.1 Hz, 2H; Ar H), 7.40 - 7.29 (m, 8H; Ar H), 7.17 (dt, J = 8.5, 4.4 Hz, 2H; Ar H), 7.08 (d, J = 6.9 Hz, 4H; Ar H), 6.97 (d, J = 4.2 Hz, 4H; Ar H), 6.64 (d, J = 8.2 Hz, 2H; Ar H); MALDI-TOF MS (mass m/z): calcd for

$C_{47}H_{27}N_5$, 661.23; found, 661.98 [M^+]. Calcd(%) for $C_{47}H_{27}N_5$: C, 85.30; H, 4.11; N, 10.58. found: C, 85.32; H, 4.10; N, 10.57.

Synthesis of 3-(4-(9,9-dimethylacridin-10(9H)-yl)phenyl)acetonaphtho[1,2-b]pyrazine-8,9-dicarbonitrile (DMAC-AP):

DMACB (1.65 g, 5 mmol), APBr (1.83 g, 5.5 mmol) and palladium tetrakis(triphenylphosphine) (173 mg, 0.15 mmol) were added to a 100 mL round-bottomed flask, followed by 40 mL of toluene and 20 mL of potassium carbonate solution at a concentration of 2.0 M. The reaction was carried out at reflux for 36 h under nitrogen protection at 90 °C. The reaction was extracted three times directly with dichloromethane solution at the end of the reaction, and the organic layers were combined and concentrated, followed by column chromatographic separation (eluent was petroleum ether: dichloromethane = 1:1). The crude product was recrystallized in ethanol and dried to give an orange solid (1.96 g, 73% yield). ^{1}H NMR (500 MHz, CD_2Cl_2, 25 °C, TMS) δ (ppm): 8.71 (d, J = 7.3 Hz, 1H; Ar H), 8.67 (d, J = 7.0 Hz, 1H; Ar H), 8.61 (d, J = 8.4 Hz , 1H; Ar H), 8.61 (d, J = 8.4 Hz, 1H; Ar H), 8.62 (d, J = 8.4 Hz, 1H; Ar H), 8.14 (d, J = 7.3 Hz, 1H; Ar H), 8.09 (m, 1H; Ar H), 7.99 (d, J = 8.1 Hz, 2H; Ar H), 7.62 (d, J = 6.9 Hz, 4H; Ar H), 7.06 (d, J = 4.2 Hz, 4H; Ar H), 6.48 (d, J = 8.2 Hz , 2H; Ar H), 1.76 (s, 6H); MALDI-TOF MS (mass m/z): calcd for $C_{37}H_{23}N_5$, 537.20; found, 537.31 [M^+]. Calcd(%) for $C_{37}H_{23}N_5$: C, 82.66; H, 4.31; N, 13.03. found: C, 82.68; H, 4.30; N, 13.02.

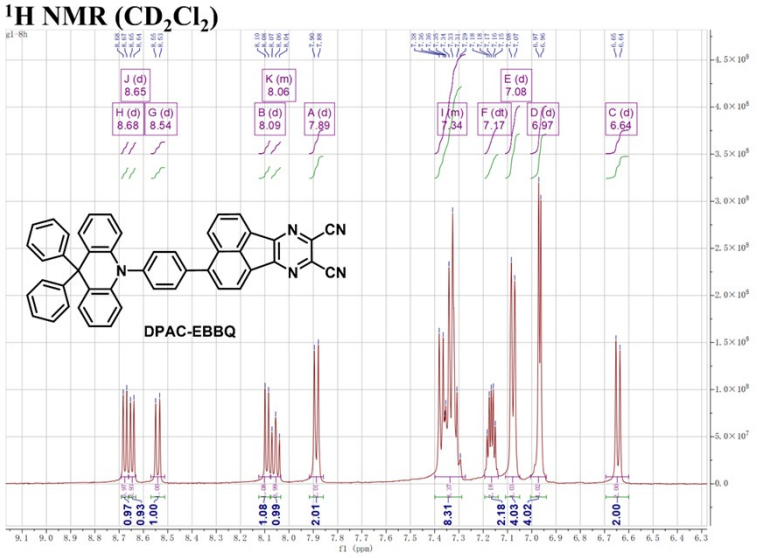

Figure S1. ^{1}H NMR spectra DPAC-AP in deuterated CD_2Cl_2.

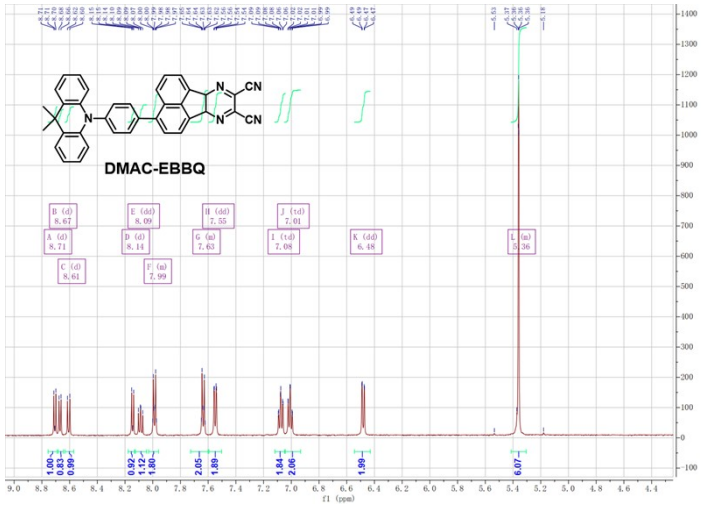

Figure S2. ^{1}H NMR spectra DMAC-AP in deuterated CD_2Cl_2.

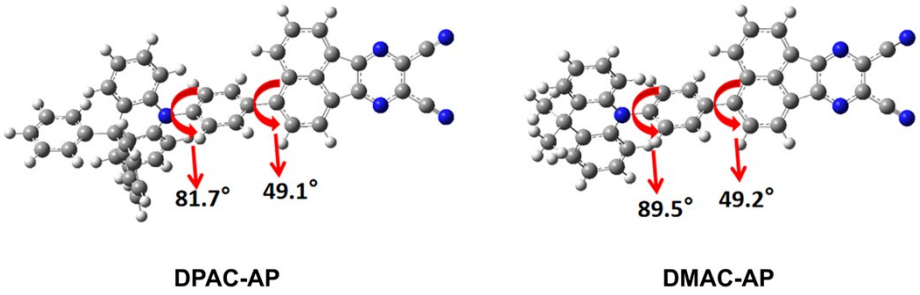

Figure S3. Optimized molecular geometries of DPAC-AP and DMAC-AP.

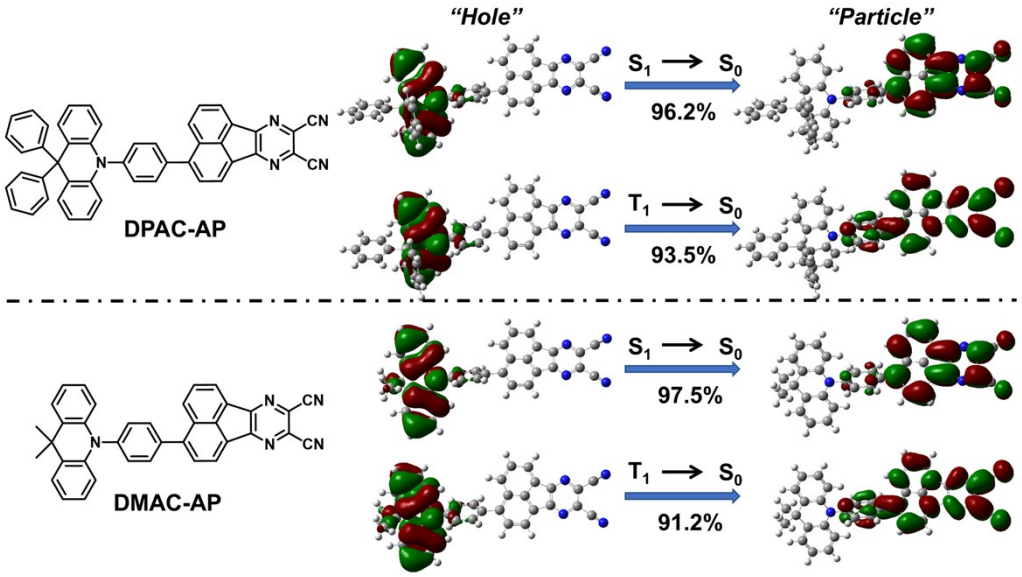

Figure S4. Natural transition orbital (NTO) analysis of DPAC-AP and DMAC-AP.

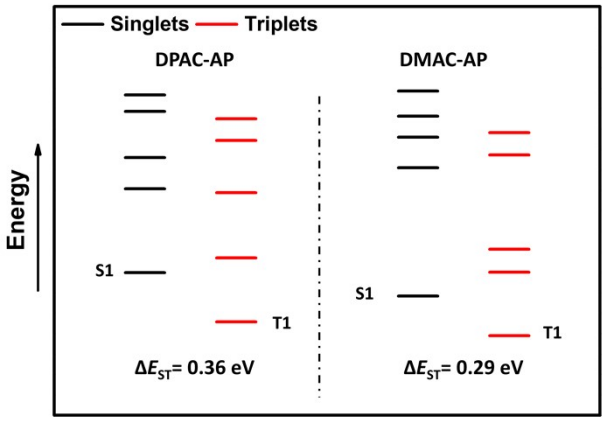

Figure S5. Energy diagram of calculated singlet and triplet excited states.

Table S1. Single crystal X-ray diffraction data of DPAC-AP and DMAC-AP.

Compound	DPAC-AP	DMAC-AP
CCDC number	2377927	2377926
Empirical formula	$C_{47}H_{27}N_5$	$C_{37}H_{23}N_5$
Formula weight	661.73	537.6
Temperature [K]	100	100
Crystal system	triclinic	monoclinic
a [Å]	8.9084(5)	20.6181(12)
b [Å]	13.3065(9)	7.3799(4)
c [Å]	27.8030(19)	18.0207(9)
α [°]	90.474(3)	90
β [°]	92.016(2)	106.096(2)
γ [°]	91.177(2)	90
Volume [Å^3]	3292.9(4)	2634.5(2)
Z	4	4
ρ_{calc} [gcm^{-3}]	1.335	1.355
μ [mm^{-1}]	0.08	0.082
F(000)	1376	1120
Goodness-of-fit on F^2	1.192	1.033
Final *R* indexes	0.0606	0.0365
[$I \geq 2\sigma(I)$]	0.1802	0.0930

Largest peak/hole [eÅ^{-3}]	0.49/−0.31	0.30/−0.21

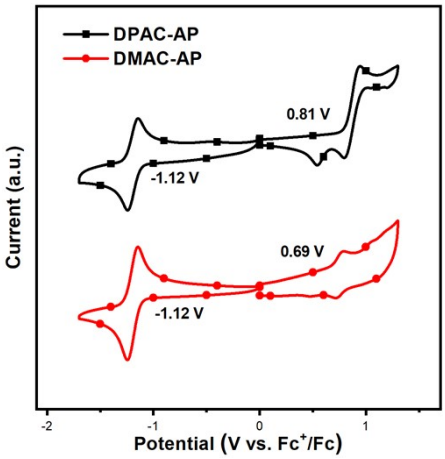

Figure S6. Cyclic voltammograms curves of DPAC-AP and DMAC-AP.

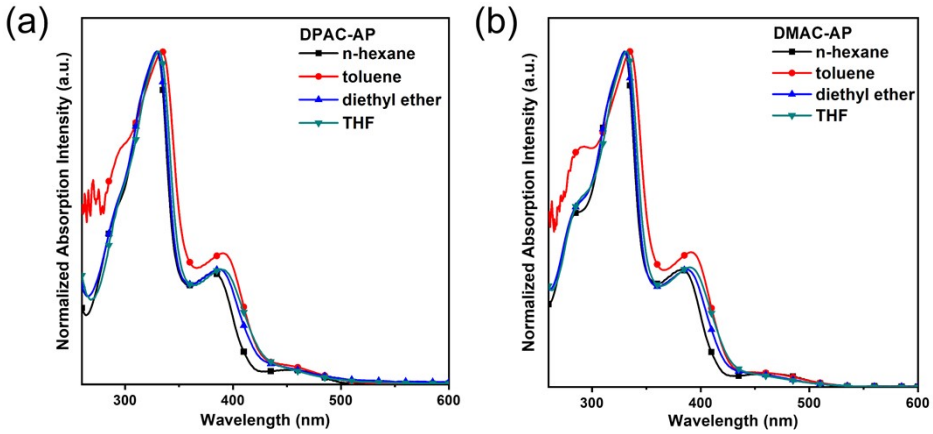

Figure S7. The absorption spectra of DPAC-AP and DMAC-AP in different solvents.

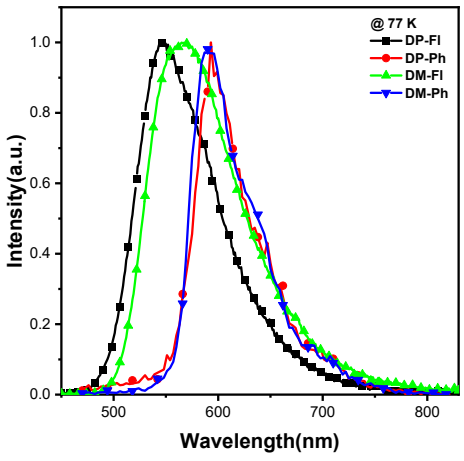

Figure S8. Low-temperature fluorescence and phosphorescence spectra at 77 K of DPAC-AP and DMAC-AP measured in frozen toluene matrix.

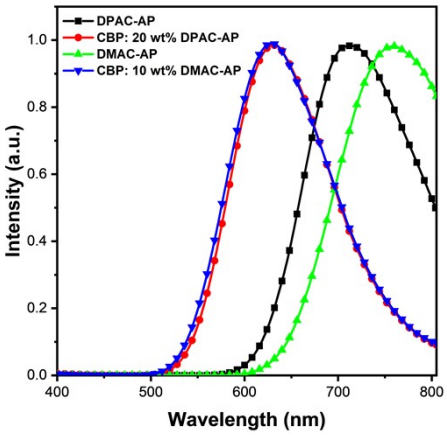

Figure S9. The PL spectra of DPAC-AP, DMAC-AP and their doped film in CBP.

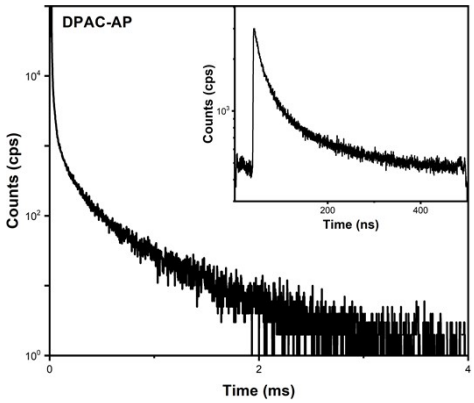

Figure S10. Transient PL decay spectra of DPAC-AP in CBP doped film.

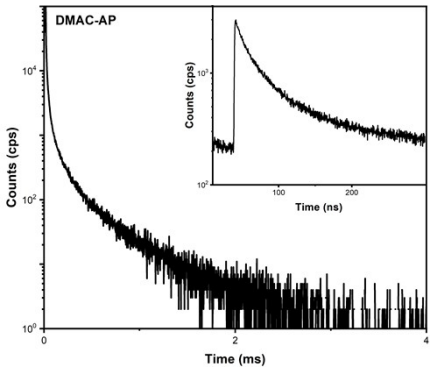

Figure S11. Transient PL decay spectra of DMAC-AP in CBP doped film.

Table S2. The kinetic parameters calculated in the doped films.

Compound	ϕ_{PL}	ϕ_p	ϕ_d	τ_p (ns)	τ_d (μs)	k_r (10^7 s^{-1})	k_{nr} (10^6 s^{-1})	k_{ISC} (10^7 s^{-1})	k_{RISC} (10^4 s^{-1})
DPAC-AP	72.2	53.4	18.7	27.0	187.9	1.98	7.65	0.96	7.18
DMAC-AP	69.0	41.7	27.3	19.3	123.2	2.18	9.64	2.04	13.39

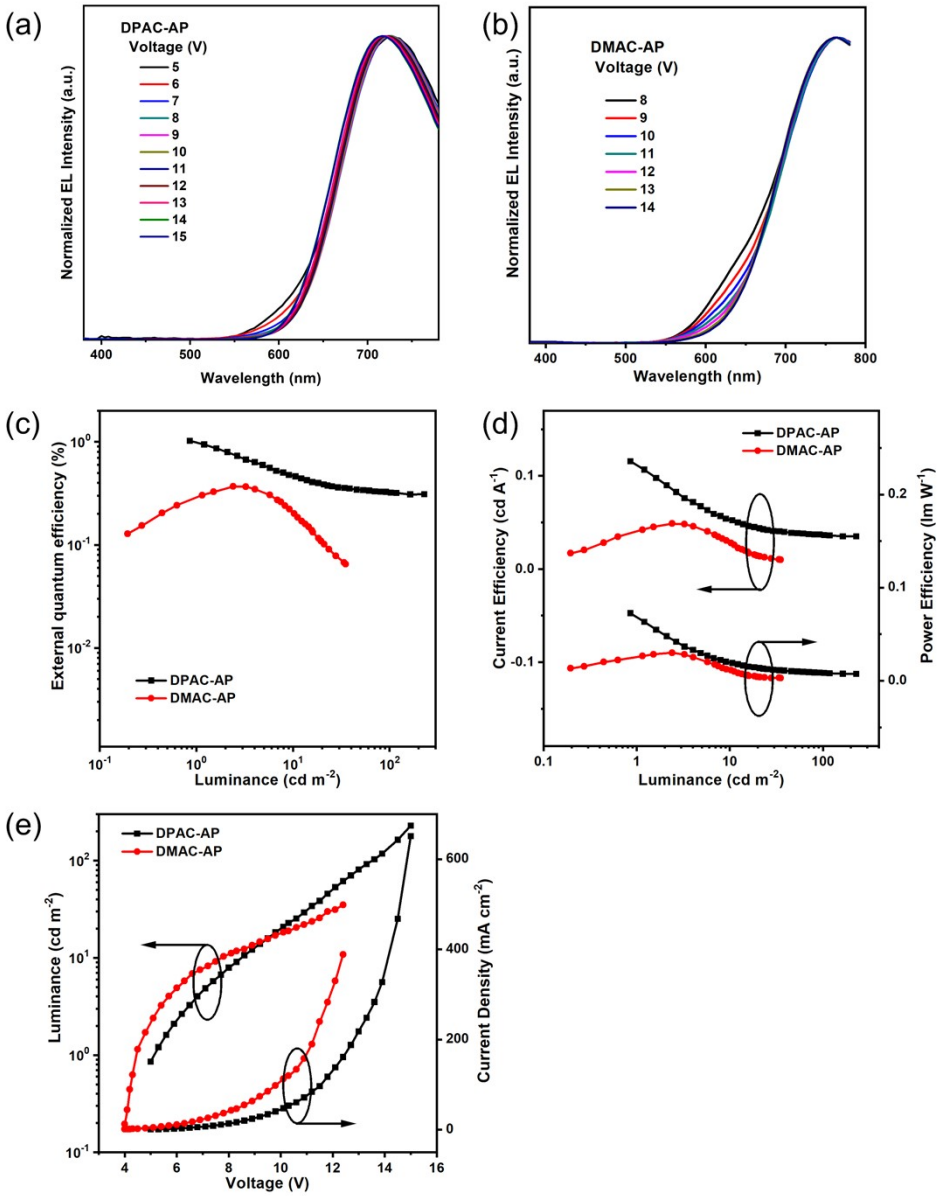

Figure S12. (a), (b) EL spectra at different voltage of DPAC-AP and DMAC-AP; (c) EQE-Luminance curve; (d) Current Efficiency-Luminance-Power Efficiency curve; (e) Luminance-Voltage-Current Density curve.

Table S3. The summary of EL performances of non-doped devices based on DPAC-AP and DMAC-AP.

Emitter	V_{on}[a]	L_{max}[b]	PE_{max}[c]	CE_{max}[d]	EQE (%)[e]		λ_{max}[f]	CIE[g]
	(V)	(cd m^{-2})	(lm W^{-1})	(cd A^{-1})	Max	100 cd m^{-2}	(nm)	(x, y)
DPAC-AP	5.0	228	0.07	0.12	1.02	0.32	720	(0.66, 0.31)
DMAC-AP	4.0	35	0.03	0.05	0.37	-	764	(0.64, 0.34)

[a] turn-on voltage at the luminescence of 1 cd m^{-2}; [b] maximum luminance; [c] maximum power efficiency; [d] maximum current efficiency; [e] external quantum efficiency at maximum/at 100 cd m^{-2}; [f] emission peak of EL spectra at 6 V; [g] Commission International de l'Eclairage (CIE) coordinates at 6 V.

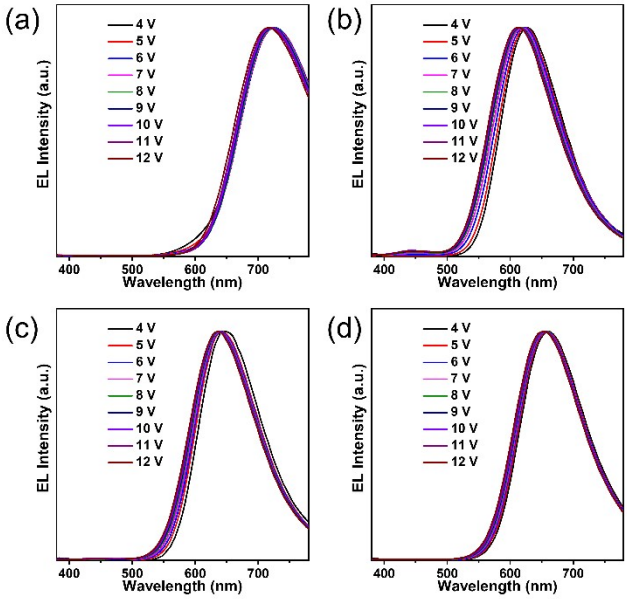

Figure S13. The EL spectra of (a) non-doped, (b) 10 wt%, (c) 20 wt% and (d) 30 wt% at different voltage of DPAC-AP.

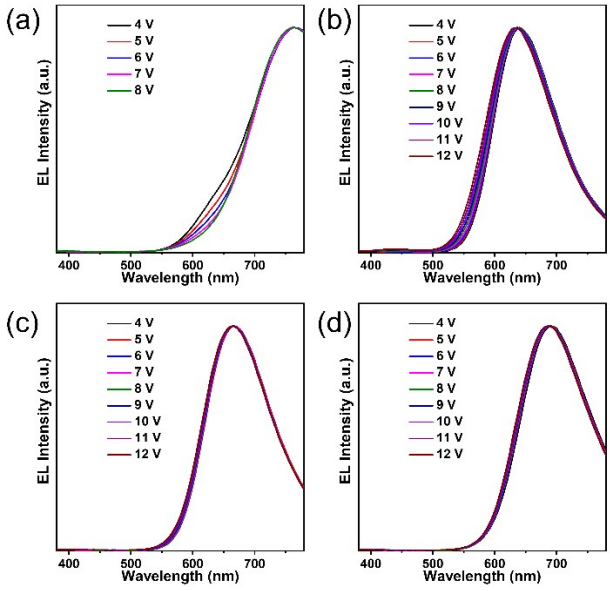

Figure S14. The EL spectra of (a) non-doped, (b) 10 wt%, (c) 20 wt% and (d) 30 wt% at different voltage of DMAC-AP.

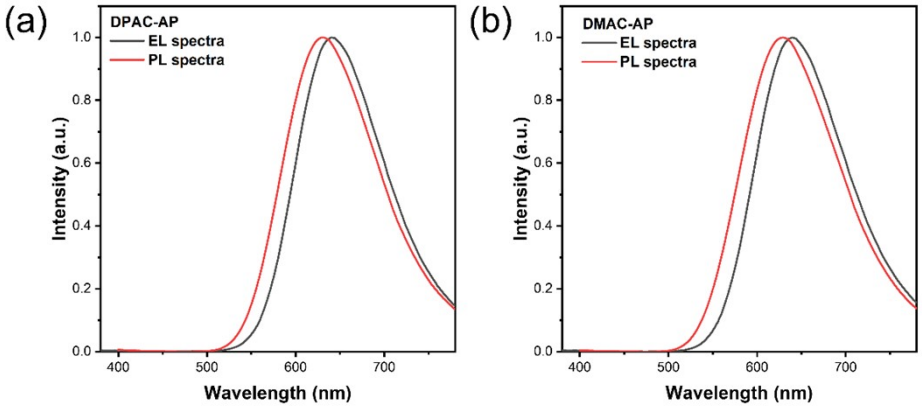

Figure S15. The comparison of EL and PL spectra in doped film.

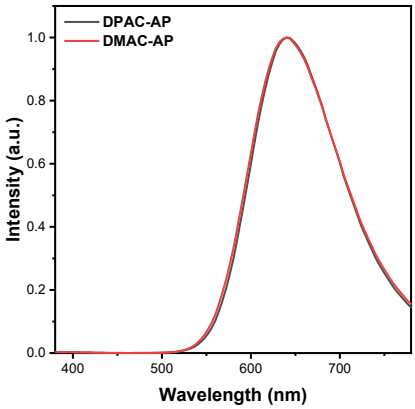

Figure S16. The EL spectra of DPAC-AP and DMAC-AP doped devices (TCTA removed).

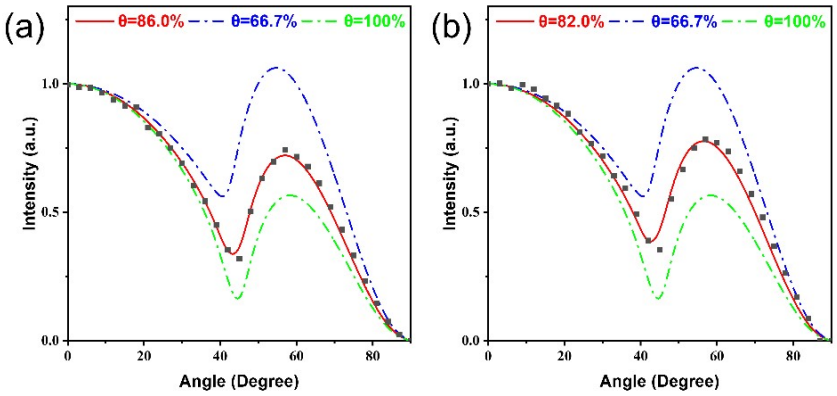

Figure S17. P-polarized PL spectra and estimated $\Theta_{//}$ values of (A) DPAC-AP and (B) DMAC-AP doped films.

In order to verify the accuracy of the devices' results, we prepared the corresponding devices with representative emitters (Alq_3[1], PO-01[2], MADN[3] and 4CzIPN[4]) as the

emitting layers, and their efficiencies were found to be highly consistent with expected values (Table S4 and Figure S18-S21).

Table S4. The summary of EL performances of Alq_3, PO-01, MADN and 4CzIPN.

Emitter	V_{on}[a] (V)	L_{max}[b] (cd m^{-2})	PE_{max}[c] (lm W^{-1})	CE_{max}[d] (cd A^{-1})	EQE_{max}[e] (%)	λ_{max}[f] (nm)	CIE[g] (x, y)
Alq_3	2.9	104024	8.24	9.70	3.23	504	(0.36, 0.53)
PO-01	3.1	201887	117.41	106.30	38.22	564	(0.50, 0.49)
MADN	3.4	9536	1.97	2.49	2.64	436	(0.15, 0.10)
4CzIPN	3.1	69714	82.58	75.11	25.68	516	(0.28, 0.56)

[a] turn-on voltage at the luminescence of 1 cd m^{-2}; [b] maximum luminance; [c] maximum power efficiency; [d] maximum current efficiency; [e] external quantum efficiency at maximum/at 1000 cd m^{-2}; [f] emission peak of EL spectra at 6 V; [g] Commission International de l'Eclairage (CIE) coordinates at 6 V.

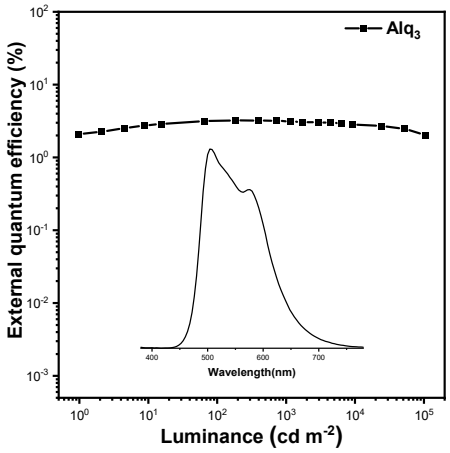

Figure S18. The external quantum efficiency curves (inset: the EL spectra) of Alq_3 with the device structure of ITO/HAT-CN (6 nm)/TAPC (25 nm)/TCTA (15 nm)/ Alq_3 (20 nm)/TmPyPB (40 nm)/LiF (1 nm)/Al (120 nm).

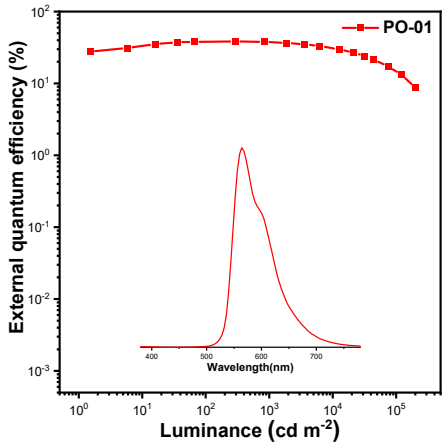

Figure S19. The external quantum efficiency curves (inset: the EL spectra) of PO-01 with the device structure of ITO/HAT-CN (6 nm)/TAPC (25 nm)/TCTA (15 nm)/ CBP:5 wt% PO-01 (20 nm)/TmPyPB (40 nm)/LiF (1 nm)/Al (120 nm).

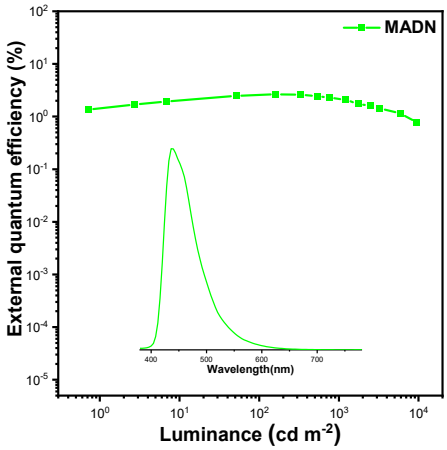

Figure S20. The external quantum efficiency curves (inset: the EL spectra) of MADN with the device structure of ITO/HAT-CN (6 nm)/TAPC (25 nm)/TCTA (15 nm)/ MADN (20 nm)/TmPyPB (40 nm)/LiF (1 nm)/Al (120 nm).

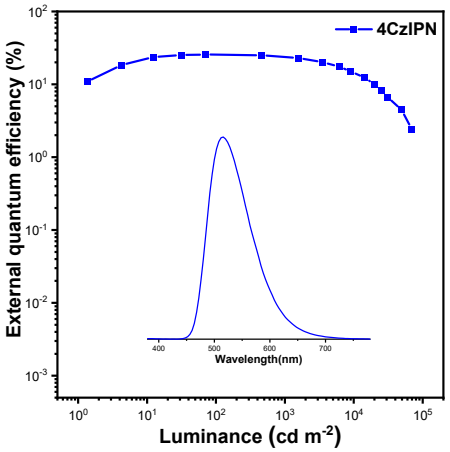

Figure S21. The external quantum efficiency curves (inset: the EL spectra) of 4CzIPN with the device structure of ITO/HAT-CN (6 nm)/TAPC (25 nm)/TCTA (15 nm)/

CBP:5 wt% 4CzIPN (20 nm)/TmPyPB (40 nm)/LiF (1 nm)/Al (120 nm).

Table S5. EQE summary of representative deep-red TADF OLEDs with emission peaks between 630 and 700 nm.

Emitter	V_{on} (V)	λ_{EL} (nm)	$EQE_{max/100}$ (%)	CIE (x, y)	Reference
DPAC-AP	2.9	640	14.1/8.3	(0.63, 0.36)	This work
DMAC-AP	2.6	640	14.4/8.0	(0.62, 0.36)	This work
TPA-QCN	3.0	644	14.3/2.5	(0.62, 0.38)	[5]
TIQD	3.2	666	12.7/-	(0.68, 0.32)	[6]
T-β-IQD	3.0	672	15.9/-	(0.68, 0.32)	[6]
pTPA-DPPZ	7	652	12.3/11.9	(0.67, 0.33)	[7]
CNPP-TPA	4.0	684	8.7/-	(0.68,0.31)	[8]
DACz-BPCN	-	631	11.0/-	(0.60, 0.39)	[9]
DBPz-2spAc	2.9	637	13.3/-	(0.60, 0.39)	[10]
DPXZ-DPPM	3.6	630	11.5/-	(0.61, 0.38)	[11]
TCPQ	2.6	642	18.5/9.7	(0.65, 0.34)	[12]
APPT-PXZ	3.0	640	7.2/-	(0.65, 0.35)	[13]
CN-TPA	3.1	688	22.8/1.0	(0.68, 0.32)	[14]
TPXZ-QX	-	637	13.8/-	(0.63, 0.36)	[15]
TPXZ-2QX	-	662	11.4/-	(0.61, 0.34)	[15]
OBN-3CN	2.9	646	19.7/-	(0.63,0.37)	[16]
*t*BuTPA-CNQx	-	648	17.4/-	(0.64, 0.35)	[17]

References:

1. C. W. Tang and S. A. V. Slyke, *Appl. Phys. Lett.*, 1987, **51**, 913-915.

2. S.-Y. Huang, H.-F. Meng, H.-L. Huang, T.-C. Chao, M.-R. Tseng, Y.-C. Chao and S.-F. Horng, *Synth. Met.*, 2010, **160**, 2393-2396.

3. M.-T. Lee, H.-H. Chen, C.-H. Liao, C.-H. Tsai and C. H. Chen, *Appl. Phys. Lett.*, 2004, **85**, 3301-3303.

4. H. Uoyama, K. Goushi, K. Shizu, H. Nomura and C. Adachi, *Nature*, 2012, **492**,

234-238.

5. C. Li, R. Duan, B. Liang, G. Han, S. Wang, K. Ye, Y. Liu, Y. Yi and Y. Wang, *Angew. Chem. Int. Ed.*, 2017, **56**, 11525-11529.

6. M. Zhao, M. Li, W. Li, S. Du, Z. Chen, M. Luo, Y. Qiu, X. Lu, S. Yang, Z. Wang, J. Zhang, S. J. Su and Z. Ge, *Angew. Chem. Int. Ed.*, 2022, **61**, e202210687.

7. B. Zhao, H. Wang, C. Han, P. Ma, Z. Li, P. Chang and H. Xu, *Angew. Chem. Int. Ed.*, 2020, **59**, 19042-19047.

8. H. Wang, B. Zhao, C. Qu, C. Duan, Z. Li, P. Ma, P. Chang, C. Han and H. Xu, *Chem. Eng. J.*, 2022, **436**, 135080.

9. S. Kothavale, W. J. Chung and J. Y. Lee, *J. Mater. Chem. C*, 2020, **8**, 7059-7066.

10. K. Zhang, X. Zhang, J. Fan, Y. Song, J. Fan, C.-K. Wang and L. Lin, *J. Phys. Chem. Lett.*, 2022, **13**, 4711-4720.

11. J. Liang, C. Li, Y. Cui, Z. Li, J. Wang and Y. Wang, *J. Mater. Chem. C*, 2020, **8**, 1614-1622.

12. Y. Liu, J. Yang, Z. Mao, X. Chen, Z. Yang, X. Ge, X. Peng, J. Zhao, S.-J. Su and Z. Chi, *ACS Appl. Mater. Interfaces*, 2022, **14**, 33606-33613.

13. W. Yang, W. Ning, S. Gong and C. Yang, *Dyes Pigm.*, 2021, **192**, 109474.

14. J.-L. He, F.-C. Kong, B. Sun, X.-J. Wang, Q.-S. Tian, J. Fan and L.-S. Liao, *Chem. Eng. J.*, 2021, **424**, 130470.

15. X.-F. Song, C. Jiang, N. Li, J. Miao, K. Li and C. Yang, *Chem. Sci.*, 2023, **14**, 12246-12254.

16. B. Sun, L. Ding, X. Wang, Z.-L. Tu and J. Fan, *Chem. Eng. J.*, 2023, **476**, 146511.

17. S. Kothavale, S. C. Kim, K. Cheong, S. Zeng, Y. Wang and J. Y. Lee, *Adv. Mater.*, 2023, **35**, 2208602.